Molecular-field-coefficient modeling of temperature-dependent ferrimagnetism in a complex oxide

Miela J. Gross,[1,*] Tingyu Su,[2] Jackson J. Bauer,[3] and Caroline A. Ross[3,†]

[1]*Department of Electrical Engineering and Computer Science, Massachusetts Institute of Technology, Cambridge, Massachusetts 02139, USA*

[2]*Department of Mechanical Engineering, Massachusetts Institute of Technology, Cambridge, Massachusetts 02139, USA*

[3]*Department of Materials Science and Engineering, Massachusetts Institute of Technology, Cambridge, Massachusetts 02139, USA*

The temperature-dependent magnetic moment of a magnetically ordered material is fundamental to all aspects of its technological applications. In ferrimagnetic materials with multiple sublattices containing different magnetic ions, the magnetization can vary nonmonotonically with temperature. Computational modeling of these materials provides insight into their sublattice occupancy and prediction of their behavior as a function of composition. Here we develop a PYTHON computer code called DIONNE that models the magnetism of rare earth (RE) iron garnets ($RE_3Fe_5O_{12}$, REIGs) using molecular field coefficient theory. The program calculates the exchange interactions and the magnetic moment of each sublattice to determine the net magnetization and angular momentum as a function of temperature. DIONNE accounts for site occupancy on each sublattice, including the effects of nonmagnetic and magnetic substitutions, vacancies, Fe^{2+}, and deviations from the ideal RE:Fe stoichiometry by considering their effects on the magnetization and exchange coupling. Unlike previous iterative methods, DIONNE recursively solves for the moment at each temperature, yielding an excellent match to magnetization versus temperature data for a range of bulk garnets. This work predicts magnetic properties of REIGs with a variety of compositions and point defect levels and enables design of ferrimagnets with useful properties.

I. INTRODUCTION

Ferrimagnetic materials consist of two or more magnetic sublattices with antiparallel coupling, leading to behavior that differs qualitatively from that of ferromagnets. For example, ferrimagnets may show magnetization and angular momentum compensation temperatures, dynamics that resemble those of antiferromagnets, and sublattice-specific optical or electronic properties [1,2]. Ferrimagnets have been used in a range of data storage, logic, photonic, signal processing, and sensor devices taking advantage of their spintronic, magneto-optical and microwave properties [1–6]. Ferrimagnetic oxides, particularly yttrium iron garnet, exhibit low Gilbert damping [7–10] and high resistivity [11–13]. Furthermore, thin films of iron garnets can be grown with perpendicular magnetic anisotropy which is desirable for many spintronic device applications [14–16]. Predicting and explaining the temperature-dependent magnetization is essential in optimizing garnets and other ferrimagnets for specific applications.

The molecular field theory of Néel [17] has been used successfully to model ferrimagnetic materials [18–20]. The magnetization is separated into contributions from the magnetic species on each sublattice, whose temperature dependence is represented by Brillouin functions. This, combined with the appropriate molecular field coefficients (MFCs) to model the intra- and intersublattice exchange coupling strength, yields the net magnetic moment as a function of temperature. Dionne [19,21–25] applied this theory to yttrium iron garnet and rare earth (RE) iron garnets (REIGs, $RE_3Fe_5O_{12}$) and obtained a good quantitative fit to experimental data of magnetization versus temperature, $M(T)$ [26–35]. This model addressed a full range of RE substituents as well as limited ranges of nonmagnetic substitutions for Fe. It does not account generally for nonideal site occupancies such as RE or Fe antisite defects. Modeling the effects of such defects is particularly important for understanding thin-film ferrimagnet properties because epitaxial growth can stabilize films with compositions far from those of bulk crystals [36].

Here we develop a computer program in PYTHON, named DIONNE after our colleague Dr. Gerald F. Dionne [37], which models the magnetic moment and angular

---

momentum of REIGs as a function of temperature. The program accounts for a wide range of site occupancies in REIGs, including nonmagnetic and magnetic substitutions, vacancies in all sublattices, Fe^{2+} substitutions, and deviations from the ideal RE:Fe $= 3:5$ stoichiometry. While prior models calculate the moment iteratively [25,38], DIONNE recursively solves for the moment and angular momentum which increases the accuracy of the model up to the Curie temperature. We validate the model by comparison with data from bulk stoichiometric REIGs as well as those with mixed RE elements and nonmagnetic substitutions. We then model REIGs with large deviations from bulk stoichiometry, in particular Tb-rich TbIG, which enables determination of sublattice occupancy. While DIONNE is used here for REIGs, the approach can be adapted to model $M(T)$ for other multi-sublattice ferrimagnetic oxides such as spinels [39,40].

II. DESCRIPTION OF MODEL

REIGs comprise three cation sublattices: tetrahedral Fe^{3+} (d-sites), octahedral Fe^{3+} (a-sites), and dodecahedral RE^{3+} (c-sites), in the ratio of 3:2:3 sites per formula unit of $RE_3Fe_5O_{12}$. The strongest coupling is antiferromagnetic superexchange between the Fe in the a- and d-sites, and the c-sites are also coupled antiferromagnetically to the d-site sublattice. Thus, the magnetic moment M of the REIG is the absolute value of the d-site moment minus the a-site and c-site moments,

$$M = |M_d - M_a - M_c|, \quad (1)$$

where M_d, M_a, and M_c are the moments of the d-, a-, and c-site sublattices, respectively. Following Dionne [19,21–25], we utilize the molecular field theory of Néel [17], which combines the use of MFCs and Brillouin functions to model the magnetic behavior. Each sublattice moment is the product of the zero-temperature moment, controlling the amplitude, and a Brillouin function, giving the moment as a function of temperature according to the S, L, J quantum numbers of the ions occupying the sublattice and the exchange field due to neighboring ions. At a given temperature, T, the moment of sublattice $M_{i,T}$ (where i represents the a-, d-, or c-site) is expressed as

$$M_{i,T} = M_{i0}B_i(x_{i,T}), \quad (2)$$

in which M_{i0} is the zero-temperature moment of the i-site, $M_{i0} = nJ_ig_i\mu_BN_A$ (per mole), where n is the number of sites per formula unit (2 for d-sites and 3 for a- and c-sites), J_i is the total angular momentum, g_i is the Landé g-factor of the ion in the i-site, μ_B is the Bohr magneton, and N_A is Avogadro's number. The T-dependence is described by B_i,

the Brillouin function for the sublattice, with argument $x_{i,T}$,

$$B_i(x_{i,T}) = \left[\frac{2J_i + 1}{2J_i}\right] \coth\left[\frac{2J_i + 1}{2J_i}x_{i,T}\right]$$
$$- \left[\frac{1}{2J_i}\right] \coth\left[\frac{1}{2J_i}x_{i,T}\right],$$

where

$$x_{i,T} = \frac{J_ig_i\mu_B\mu_0}{kT} \sum_{j=a,d,c} N_{ij}M_{j,T} \quad (3)$$

in which N_{ij} represents the MFC between the i- and j-sites.

The MFCs N_{ij} quantify the exchange coupling both within a sublattice and between sublattices: N_{ij} is proportional to the exchange coupling J_{ij}. A negative sign on N_{ij} indicates parallel (ferromagnetic) coupling whereas a positive sign indicates antiparallel coupling. Superexchange between the Fe^{3+} ions in the a- and d-sites of iron garnets is described with an MFC of $N_{ad} = 97$ mol cm^{-3} [19]. The intrasublattice couplings within the a- and d-sublattices are the next strongest, with $N_{aa} = -65$ mol cm^{-3} and $N_{dd} = -30.4$ mol cm^{-3} [19]. Coupling between Fe^{3+} and RE^{3+} is an order of magnitude smaller: N_{ac} and N_{cd} are shown in Table S1 in the Supplemental Material for various c-site REs which came from fitting experimental data [25,31,66]. The coupling between REs in the c-sites is negligible: N_{cc} is taken as zero. The model does not account for spin reorientation or noncollinear magnetic order [41,42].

Although the MFC model has been previously implemented for a range of bulk iron garnets [18–20,25,38, 43–49], to our knowledge, MFC modeling has not been optimized for materials with nonideal site occupancies such as antisite Fe or antisite RE. Furthermore, evaluating the Brillouin function is computationally demanding, requiring multiple sinusoidal functions, and each sublattice moment depends on the other sublattices, resulting in a system of nonlinear equations. Our previous model [38] and Dionne's model written in Fortran [25] iteratively solved this system of equations by calculating the magnetization at each temperature from the sublattice moments at lower temperatures, creating inaccuracies at higher temperatures. DIONNE recursively solves this system of equations at each temperature using fsolve in the optimize section of the SCIPY PYTHON library [50]. DIONNE is implemented in PYTHON to minimize both runtime and memory requirements for efficient processing. DIONNE is available on GitHub at [51].

III. RESULTS AND DISCUSSION

A. REIGs with one or more rare earth element

We first model REIGs with one RE to validate the approach. Table S1 in the Supplemental Material [66]
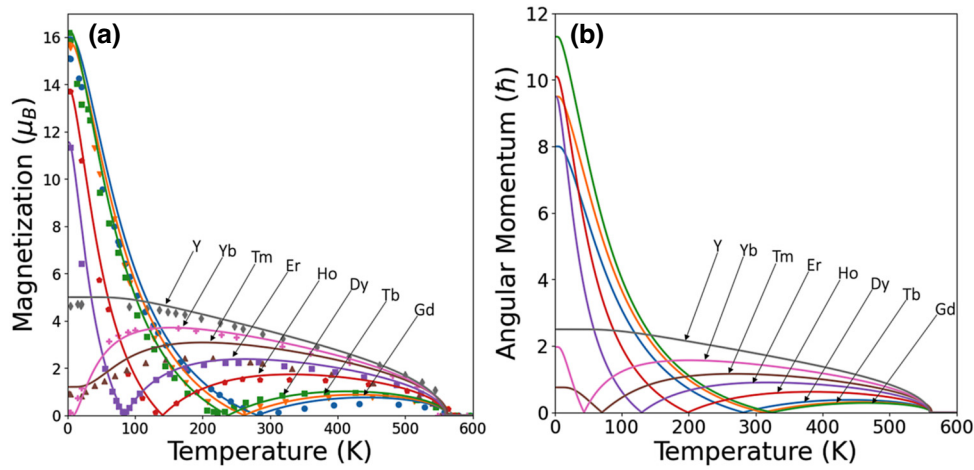
FIG. 1.   Magnetic moment (a) and angular momentum (b) versus temperature curves of eight different REIGs, with each curve color corresponding to the indicated RE. In (a), lines are from our model and data points from Pauthenet [35]. Further comparisons with both experimental data [25,28,30,35,53] and Dionne's model [25] are shown in Fig. S1 in the Supplemental Material [66]. Magnetization is plotted in units of μ_B per formula unit (f.u.), angular momentum is in units of $h/2\pi$ per formula unit.

provides the angular momentum, Landé g-factor, and MFCs of each RE in the c-site, derived from theory and experimental fitting [20,25,31,35,52]. Figure 1(a) shows the resulting plots for several different REIGs, each with one RE, compared with the experimental results from Pauthenet [35]. Figure S1 in the Supplemental Material shows additional examples plotted with past experimental and modeled results [25,28,30,31,35,53,66]. Inconsistencies between different experimentally reported results slightly alter the moment versus temperature curves, which can be accounted for with small modifications to the values in Table S1 in the Supplemental Material [66]. The Curie temperature T_C is dominated by the coupling between the Fe on the a- and d-sites and is 560 K, independent of the RE, in agreement with experimental data [31,34,35]. A compensation temperature T_{comp} occurs for some REIGs where the net magnetic moment is zero. $T_{\text{comp}} = 85$ K for ErIG, increasing to $T_{\text{comp}} = 282$ K for GdIG in agreement with previously reported results [31,35,49]. Supplemental Material Note 1 [66] shows an excellent agreement of the model with experimental data.

In addition to the magnetization, DIONNE calculates the angular momentum as a function of temperature. This additional output is readily calculated from the magnetic moment and the Landé g-factors of each cation. Some REIG compositions yield an angular momentum compensation temperature, T_A, as shown in Fig. 1(b). T_A is important in determining the magnetization dynamics, for example the domain wall mobility in RE-transition metal alloys is maximum at T_A rather than at T_{comp} [54,55]. For GdIG, $T_A = T_{\text{comp}} = 282$ K because all the cations, Gd^{3+} and Fe^{3+}, have the same $g = 2$ [56]. In contrast, Er^{3+} has $g = 1.38$ and ErIG has $T_A = 130$ K, which is almost 50 K higher than its T_{comp}.

The properties of REIGs can be tuned by substitution of other REs on the c-sites. Coupling within the dodecahedral sublattice is negligible because there are no c-site nearest neighbors ($N_{cc} = 0$). This allows us to model the c-site as an average of the occupying REs, following Dionne [25]. Figure 2 shows magnetization versus temperature of two different solid solutions, Gd-substituted YIG ($Gd_xY_{3-x}Fe_5O_{12}$), Fig. 2(a), and Gd-substituted DyYIG ($Gd_xDy_{0.3}Y_{2.7-x}Fe_5O_{12}$), Fig. 2(b). YIG has no compensation temperature, but adding Gd produces a T_{comp} for $x > 0.6$ Gd per formula unit (f.u.) in $Gd_xY_{3-x}Fe_5O_{12}$ and $x > {\sim}0.3$ in $Gd_xDy_{0.3}Y_{2.7-x}Fe_5O_{12}$. The calculated $M(T)$ matches experimental data [26,29,32] (see Supplemental Material Fig. S2 [66]).

Figure 3 compares the sublattice magnetization and angular momentum of $Dy_1Gd_2Fe_5O_{12}$, yielding $T_{\text{comp}} = 267$ K and $T_A = 296$ K. Figure 3(c) evaluates T_{comp} and T_A of DyGdIG versus composition for increasing amounts of Dy. The difference between the compensation temperatures ($T_A - T_{\text{comp}}$) increases with Dy substitution as the average g-factor of the dodecahedral sites is reduced.

B. Point defects and nonbulk stoichiometry in rare earth iron garnets

Vacancies and nonmagnetic substitutions have a large impact on the magnetic behavior of REIGs. Dionne [19] proposed that in YIG the zero-temperature magnetic moment and the MFCs of each Fe sublattice are affected by nonmagnetic substitutions in both the Fe sublattices. Thus, M_{a0}, M_{d0}, N_{aa}, N_{ad}, and N_{dd} become functions of the fraction of nonmagnetic species (including vacancies) both in the a-site, k_a, and in the d-site, k_d, where $0 \leq k_d$, $k_a < 1$. Dionne's model included a linear scaling of M_{a0} with ($1-k_a$) and M_{d0} with ($1-k_d$)
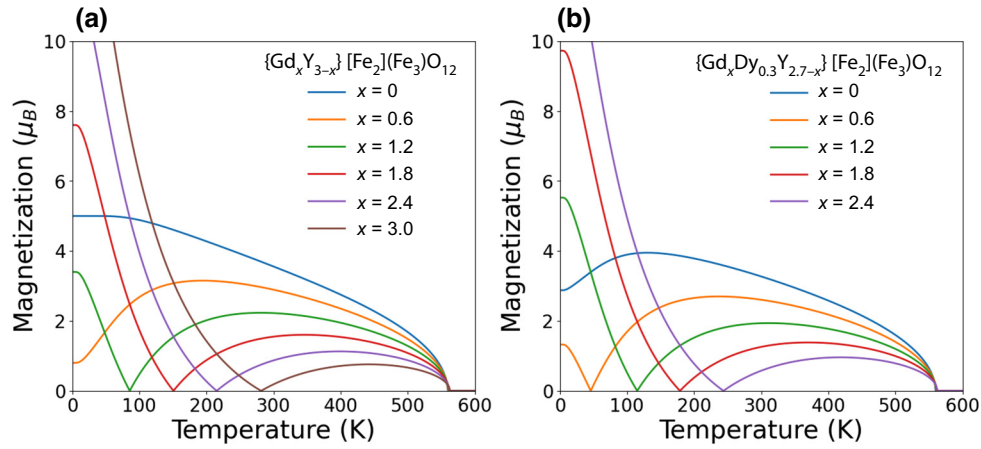
FIG. 2.   Magnetization versus temperature curves of REIGs GdYIG (a) and GdDyYIG (b). x represents the amount of Gd substituted into (a) YIG and (b) DyYIG with 0.3 Dy/f.u.

which diverged from experimental results. The deviation was attributed to canting of the magnetic moments of the nonsubstituted sublattice and was accounted for by including an empirical dependence of M_{a0} on $(1 - k_d^{5.4})$ and of M_{d0} on $(1 - 0.1k_a)$ [19]. This method fits experimental data below the antiferromagnetic transition $0 \leq k_d < 0.65$, $0 \leq k_a < 0.35$. The fraction of nonmagnetic species in the c-site, k_c, is included by linearly scaling M_{c0} with $(1-k_c)$ [25]. We adopted Dionne's expressions which are given in Supplemental Material Note 2 [19,66], modifying them to include antisite defects and divalent Fe as described in the remainder of this section.

Figures 4(a) and 4(b) show magnetization versus temperature of YIG with increasing levels of octahedral and tetrahedral nonmagnetic species, respectively. Nonmagnetic species on either site dilute the superexchange between the Fe on the a and d sublattices by reducing

the number of magnetic neighbors, and frustration of spins adjacent to the substituted site leads to spin canting and a reduction in the sublattice moment [21]. Nonmagnetic substitutions therefore reduce T_C and the values of the MFCs. However, octahedral and tetrahedral nonmagnetic species have opposing effects on the low temperature net magnetization M_0: increasing k_a raises M_0 by reducing the moment of the minority sublattice, whereas increasing k_d lowers M_0. Figure 4(c) shows the special case of antiferromagnetic YIG where one-third of the tetrahedral Fe is replaced by a trivalent nonmagnetic substituent, yielding a Néel temperature of 440 K. Figures 5(a) and 5(b) shows the agreement of DIONNE with experimental data [57].

The Fe in REIGs is trivalent, but oxygen deficiency or tetravalent cations promote the formation of Fe^{2+} for charge balance [58,59]. As a larger ion than Fe^{3+}, the Fe^{2+} preferentially occupies the octahedral sites. DIONNE can account for a-site Fe^{2+} (4 μ_B) replacing Fe^{3+} (5 μ_B) by
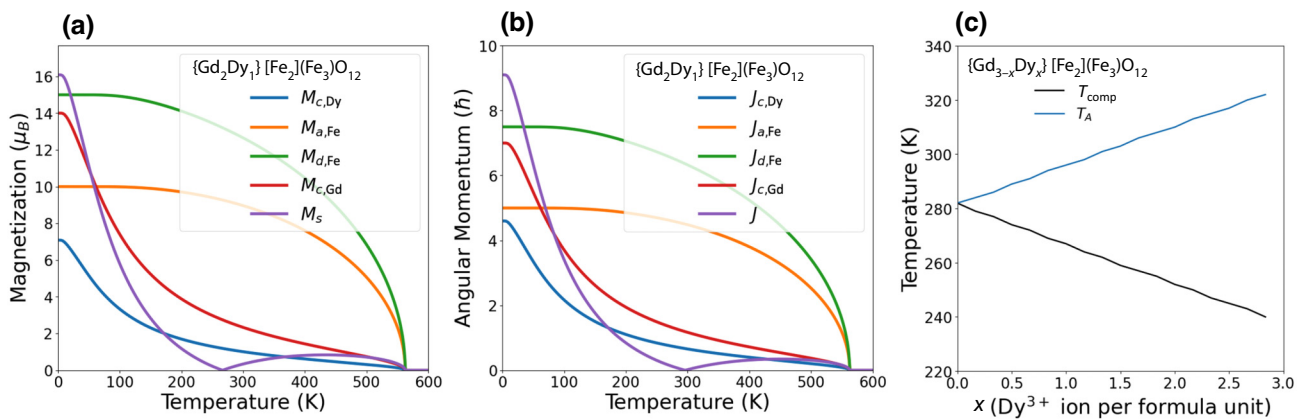

FIG. 3.   Magnetic modeling of DyGdIG. (a) Magnetization and (b) angular momentum versus temperature curve of $Dy_1Gd_2Fe_5O_{12}$ for the individual sublattices and the total per f.u. (c) Magnetic compensation and angular momentum compensation versus composition.
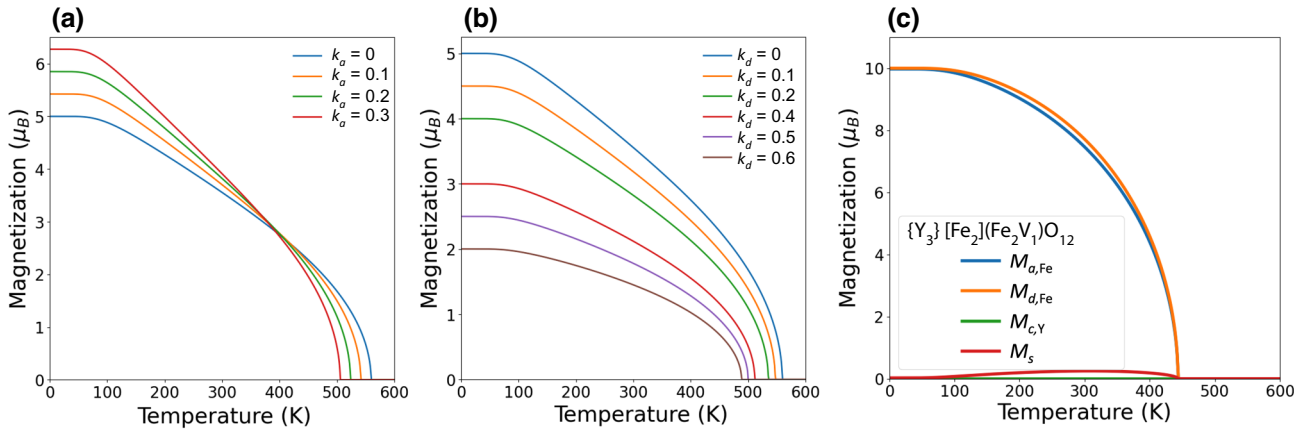
FIG. 4.   Magnetization versus temperature curves for (a) octahedral and (b) tetrahedral vacancies or nonmagnetic substitutions in YIG. (c) Antiferromagnetic YIG is simulated by substituting one-third of the tetrahedral Fe with a nonmagnetic species or vacancy V, assumed trivalent for charge balance. Since the coupling in the d-sites and a-sites differs, there is a small net moment between 150 and 450 K.

adjusting the zero-temperature magnetic moment of the a-site sublattice M_{a0} (see Supplemental Material Note 2 [66]) while using the same MFC values for Fe^{2+} that were used for Fe^{3+}. Figure 5(c) shows $M(T)$ for increasing levels of Fe^{2+} in YIG. T_C decreases as Fe^{2+} increases because Fe^{2+} lowers the octahedral sublattice moment M_{a0} and hence the intersublattice coupling, Eq. (3). Previous studies of YIG and substituted YIG containing Fe^{2+} find a decrease in T_C [58,59].

Bulk REIGs exhibit little variation from the ideal RE:Fe = 0.6 stoichiometry [60–62]. However, thin films of REIGs with compositions that deviate substantially from the ideal RE:Fe ratio can be stabilized by epitaxial growth on a garnet substrate [36]. To model these antisite defects, we consider the effects of Fe^{3+} in the c-site for Fe-rich REIGs and RE^{3+} in the a-sites for RE-rich REIGs. We

consider excess RE to occupy the a-sites and not the d-sites on steric grounds. DIONNE then needs to account for modifications in the zero-temperature moments of each sublattice, the inter- and intrasublattice MFCs, and the Brillouin functions that describe the moment of each species and sublattice.

The zero-temperature moments are taken as functions of RE in the a-sites, k_{aR}, and Fe in the c-sites, k_{cF}. The relationships are based on those developed in Ref. [19] for nonmagnetic substitutions k_a, k_d, and k_c. We assume that intrasublattice coupling is weak between the RE ions in the a-sites due to their low concentration, and similarly that coupling is weak between Fe ions in the c-sites, enabling an analogous treatment to that of multiple RE ions in the c-sites [25]. First, we create additional sublattice terms to model the antisite magnetic ions with unique MFCs. For
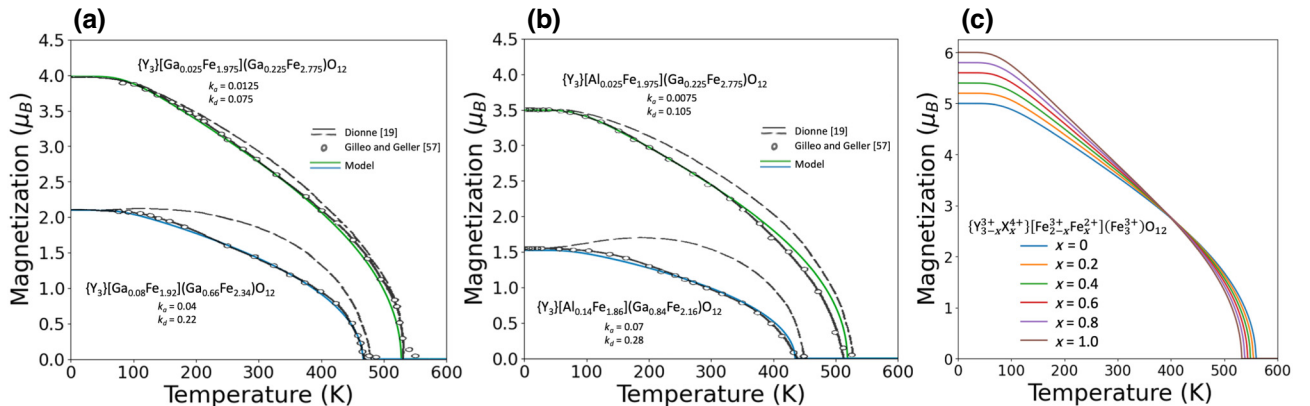

FIG. 5.   Magnetization versus temperature curves of YIG with several Fe substitutions. (a) Ga- and (b) Al-substituted YIG are plotted with the corresponding a- and d-site substitutions k_d and k_a. Model data is shown in color, compared with experimental data [57] and calculated data from Dionne [19] with (solid line) and without (dashed line) modifying the MFCs of Fe due to the nonmagnetic substitutions. (c) Fe^{2+} in octahedral sites in YIG, where X represents a nonmagnetic tetravalent ion for charge balance. (a) and (b) are adapted from [19].

excess RE we modify the zero-T moment of the a-sites by reducing the a-site Fe contribution by k_{aR}. We add back the RE contribution via a new term, M_{aR0}, which includes the J and g-factor of the RE (see Table S1 in the Supplemental Material [66]). In the case of excess Fe, we reduce the c-site RE contribution by k_{cF} and add back the Fe contribution via a new term, M_{cF0}. The general model then includes the following terms:

$$M_{d0} = 3\mu_B N_A S_F g_F (1 - k_d)(1 - 0.1(k_a + k_{aR})), \quad (4)$$

$$M_{a0} = 2\mu_B N_A[(1 - k_{F2})S_F + k_{F2}S_{F2}]g_F(1 - k_a - k_{aR})$$
$$\times \left(1 - k_d^{5.4}\right), \quad (5)$$

$$M_{aR0} = 2\mu_B N_A J'_R g_R k_{aR}(1 - k_d^{5.4}), \quad (6)$$

$$M_{c0} = 3\mu_B N_A J'_R g_R (1 - k_c - k_{cF}), \quad (7)$$

$$M_{cF0} = 3\mu_B N_A S_F g_F k_{cF}, \quad (8)$$

where g is the Landé g-factor of the respective element, J'_R is the effective angular momentum of the RE element (introduced to account for canting of the RE at low temperatures due to magnetocrystalline anisotropy [25]), and S_F and S_{F2} are the spin angular momenta of Fe^{3+} and Fe^{2+}, equal to 5/2 and 2, respectively.

Second, we modify the formulae for N_{dd}, N_{aa}, and N_{ad} to include the effects of k_{aR} and k_{cF} (see Supplemental Material Note 3 [66]), analogous to the effects of k_a and k_c [19]. N_{ac} and N_{cd} are more than an order of magnitude smaller; thus, the effects of k_{aR} and k_{cF} on them are neglected. We also introduce additional MFCs for the anti-site cations. For RE^{3+} occupying octahedral sites, N_{aaR} and N_{aRd} describe the couplings between the a-site RE^{3+} with the a-site Fe^{3+} and d-site Fe^{3+} respectively. N_{acF} (N_{cFd}) quantifies the couplings between c-site Fe^{3+} and the a-site Fe^{3+} (d-site Fe^{3+}). We neglect coupling between c-site Fe and octahedral RE ions following similar reasoning for neglecting N_{cc} (see Supplemental Material Note 4 [66]).

Initial guesses for the MFCs are based on the MFCs of the ions in their usual sites, and then further adjusted by comparison with experimental data. For example, Tb^{3+} in the dodecahedral sublattice has N_{ac} and N_{cd} of -4.2 and 6.5 mol cm^{-3}, respectively, for stoichiometric TbIG. To model Tb-rich TbIG, we initially set N_{aaR} and N_{aRd} to -4.2 and 6.5 mol cm^{-3}, respectively. These values are then fine-tuned to match experimental results as shown below.

We illustrate the application of DIONNE by fitting $M(T)$ data for a Tb-rich TbIG film reported by Rosenberg et al. [38] with $T_{comp} = 330 \pm 10$ K (higher than that of bulk TbIG, 250 K) and $T_C = 490 \pm 10$ K. X-ray photoelectron spectroscopy, transmission electron microscopy, and x-ray magnetic circular dichroism confirmed the presence of excess Tb in the octahedral sites, with Tb:Fe = 0.86, $Fe_{oct} : Fe_{tet} = 0.602$, and negligible Fe^{2+}. The $Fe_{oct} : Fe_{tet}$ ratio implies the presence of vacancies on at least the tetrahedral sites because the excess Tb occupies the octahedral sites. Our previous iterative MFC model [38] was used to determine the site occupancies by fitting only to the measured T_{comp}, yielding a stoichiometry of $\{Tb_3^{3+}\}[Fe_{1.35}V_{0.55}Tb_{0.097}^{3+}](Fe_{2.25}^{3+}V_{0.75})O_{12-\delta}^{2-}$ where $\{\}$, $[]$ and $()$ are the c-, a-, and d-sites, respectively. This stoichiometry indicates substantial concentrations of vacancies and oxygen deficiency, $\delta = 1.95$ [38], which are larger than has been reported experimentally [63].

Using DIONNE, we obtained an excellent fit to T_{comp}, T_C, and the magnetic moment of the experimental data for a composition of $\{Tb_3^{3+}\}[Fe_{1.52}Tb_{0.48}^{3+}](Fe_{2.53}^{3+}V_{0.47})O_{12-\delta}^{-2}$ as shown in Figs. 6(a) and 6(b). We arrived at this stoichiometry by first considering combinations of k_a, k_d, and k_{aR} that are consistent with the experimental data. DIONNE gave the best agreement to the experimental value of T_C when Fe vacancies were minimized. Since vacancies need only be present on the d-sites, we take $k_a = 0$, which implies $k_d = 0.47/3 = 0.16$ and $k_{aR} = 0.48/2 = 0.24$. Next, T_{comp} was fitted to the experimental data by varying
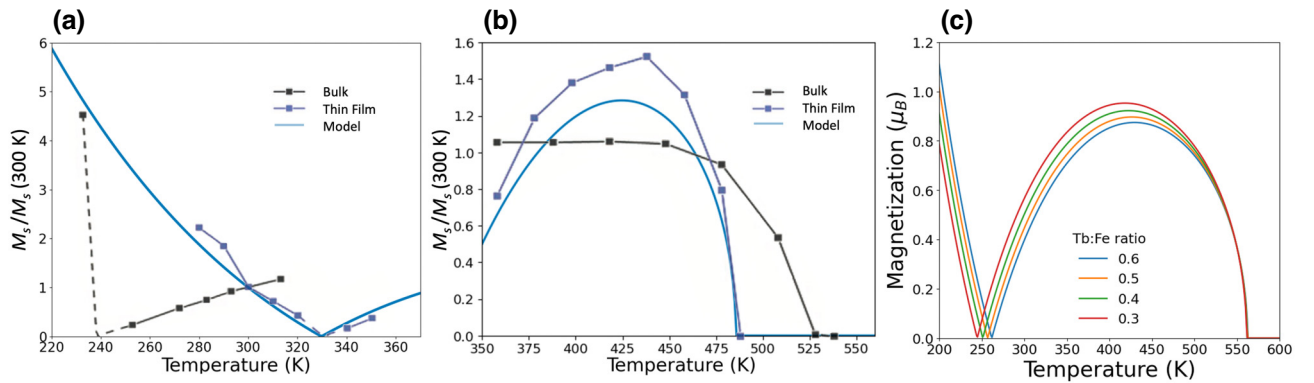

FIG. 6. Magnetization versus temperature curves of Tb-rich TbIG data reported from Rosenberg et al. [38] and DIONNE fitting the data near (a) the compensation temperature and (b) the Curie temperature. Magnetization is normalized by the moment at 300 K. (c) Magnetization versus temperature curves of Fe-rich TbIG, where excess Fe is present on the c-sites and there are no vacancies included. (a) and (b) are adapted from [38].

TABLE I.   Fit parameters for Tb-rich TbIG in Fig. 6 compared to bulk TbIG.

	Bulk TbIG	Tb-rich TbIG
k_a (fraction of vacancies on a-site)	0	0
k_d (fraction of vacancies on d-site)	0	0.16
k_{aR} (fraction of Tb on a-site)	0	0.24
N_{ad} (coupling of a-site with d-site Fe)	97 mol cm^{-3}	91.21 mol cm^{-3}
N_{aa} (coupling of a-site with a-site Fe)	-65 mol cm^{-3}	-52.17 mol cm^{-3}
N_{dd} (coupling of d-site with d-site Fe)	-30.4 mol cm^{-3}	-22.37 mol cm^{-3}
N_{cd} (coupling of c-site Tb with d-site Fe)	6.5 mol cm^{-3}	6.50 mol cm^{-3}
N_{ca} (coupling of c-site Tb with a-site Fe)	-4.2 mol cm^{-3}	-4.20 mol cm^{-3}
N_{aaR} (coupling of a-site Fe with a-site Tb)		-2.80 mol cm^{-3}
N_{aRd} (coupling of a-site Tb with d-site Fe)		8.30 mol cm^{-3}

the MFCs of the a-site Tb^{3+}, which had initially been set to the values for the c-site occupancy: $N_{ac} = -4.2$ and $N_{cd} = 6.2$ mol cm^{-3}. The best fit was obtained for $N_{aaR} = -2.8$ and $N_{aRd} = 8.3$ mol cm^{-3}. Lastly, $M(T)$ was calculated from the selected stoichiometry for the Tb-rich film which produced a good fit to the experimental data, Fig. 6. Table I shows the fit parameters for the model of the Tb-rich film and for bulk TbIG. DIONNE's best fit yields a lower vacancy concentration than the model in Ref. [38], implying a lower oxygen deficiency, $\delta = 0.31$ versus 1.95, for charge balance, which is in better agreement with other reports [63,64]. In addition, DIONNE fits T_C as well as T_{comp}, showing a better high-temperature performance than the iterative model in Ref. [38].

A complementary case is presented by Fe-rich TbIG reported in Ref. [65]. Excess Fe led to a decrease in T_{comp}, opposite to the case of Tb-rich TbIG. To model the c-site Fe, we estimate N_{acF} and N_{cFd} to be -6.5 and 9.7 mol cm^{-3}, respectively, approximately an order a magnitude smaller than N_{aa} and N_{ad}. DIONNE reproduces the experimental trend, showing T_{comp} decreasing as a function of the Tb:Fe ratio, Fig. 6(c). T_C was not reported in Ref. [65]; however, Fig. 6(c) shows T_C depends little on the Tb:Fe ratio. Instead, Fe^{3+} vacancies and substitutions have a significant effect on both T_C and T_{comp}.

IV. CONCLUSION

In summary, we developed DIONNE, a PYTHON computer program that uses MFCs to model the magnetic behavior of REIGs. The program calculates both the magnetization and angular momentum of each sublattice as functions of temperature for a REIG, yielding the compensation temperatures T_A and T_{comp} and the Curie temperature, T_C. DIONNE can also account for a wider range of point defects, substitutions, and stoichiometries than previously reported models [18–20,25,38,43–48] by considering the effects on the zero-temperature magnetization and sublattice coupling. Deviations from the RE:Fe = 3:5 stoichiometry were captured by introducing an additional sublattice moment to account for the excess Fe or RE in addition to modifying

the relevant zero-temperature moments and MFCs. Comparison with experimental data from a Tb-rich TbIG film [38] enabled the site occupancy to be fitted to give a good quantitative agreement to the measured T_{comp} and T_C and implying the existence of tetrahedral vacancies. This modeling approach will facilitate the design of ferrimagnets with useful magnetic and spintronic properties.

[1] Y. Zhang, X. Feng, Z. Zheng, Z. Zhang, K. Lin, X. Sun, G. Wang, J. Wang, J. Wei, P. Vallobra, *et al.*, Ferrimagnets for spintronic devices: from materials to applications, Appl. Phys. Rev. **10**, 011301 (2023).

[2] S. K. Kim, G. S. D. Beach, K. J. Lee, T. Ono, T. Rasing, and H. Yang, Ferrimagnetic spintronics, Nat. Mater. **21**, 24 (2022).

[3] Y. Kajiwara, K. Harii, S. Takahashi, J. Ohe, K. Uchida, M. Mizuguchi, H. Umezawa, H. Kawai, K. Ando, K. Takanashi, *et al.*, Transmission of electrical signals by spin-wave interconversion in a magnetic insulator, Nature **464**, 262 (2010).

[4] J. A. González, J. P. Andrés, and R. L. Antón, Applied trends in magnetic rare earth/transition metal alloys and multilayers, Sensors **21**, 5615 (2021).

[5] K. Srinivasan and B. J. H. Stadler, Review of integrated magneto-optical isolators with rare-earth iron garnets for polarization diverse and magnet-free isolation in silicon photonics [invited], Opt. Mater. Express **12**, 697 (2022).

[6] J. F. Barry, R. A. Irion, M. H. Steinecker, D. K. Freeman, J. J. Kedziora, R. G. Wilcox, and D. A. Braje, Ferrimagnetic oscillator magnetometer, Phys. Rev. Appl. **19**, 044044 (2023).

[7] H. Chang, P. Li, W. Zhang, T. Liu, A. Hoffmann, L. Deng, and M. Wu, Nanometer-thick yttrium iron garnet films with extremely low damping, IEEE Magn. Lett. **5**, 1 (2014).

[8] O. Ciubotariu, A. Semisalova, K. Lenz, and M. Albrecht, Strain-induced perpendicular magnetic anisotropy and

gilbert damping of $Tm_3Fe_5O_{12}$ thin films, Sci. Rep. **9,** 17474 (2019).

[9] Y. Zhao, Y. Li, S. Zhu, C. Chen, M. Yao, Y. Zhao, Z. Hu, B. Peng, M. Liu, and Z. Zhou, Voltage tunable low damping YIG/PMN-PT multiferroic heterostructure for low-power RF/Microwave devices, J. Phys. D: Appl. Phys. **54,** 245002 (2021).

[10] C. Hauser, T. Richter, N. Homonnay, C. Eisenschmidt, M. Qaid, H. Deniz, D. Hesse, M. Sawicki, S. G. Ebbinghaus, and G. Schmidt, Yttrium iron garnet thin films with very low damping obtained by recrystallization of amorphous material, Sci. Rep. **6,** 20827 (2016).

[11] C. O. Avci, E. Rosenberg, M. Baumgartner, L. Beran, A. Quindeau, P. Gambardella, C. A. Ross, and G. S. D. Beach, Fast switching and signature of efficient domain wall motion driven by spin-orbit torques in a perpendicular anisotropy magnetic insulator/Pt bilayer, Appl. Phys. Lett. **111,** 072406 (2017).

[12] S. Vélez, J. Schaab, M. S. Wörnle, M. Müller, E. Gradauskaite, P. Welter, C. Gutgsell, C. Nistor, C. L. Degen, M. Trassin, *et al.*, High-speed domain wall racetracks in a magnetic insulator, Nat. Commun. **10,** 4750 (2019).

[13] L. J. Cornelissen, J. Liu, R. A. Duine, J. Ben Youssef, and B. J. Van Wees, Long-distance transport of magnon spin information in a magnetic insulator at room temperature, Nat. Phys. **11,** 1022 (2015).

[14] L. Soumah, N. Beaulieu, L. Qassym, C. Carrétéro, E. Jacquet, R. Lebourgeois, J. Ben Youssef, P. Bortolotti, V. Cros, and A. Anane, Ultra-low damping insulating magnetic thin films get perpendicular, Nat. Commun. **9,** 3355 (2018).

[15] A. Quindeau, C. O. Avci, W. Liu, C. Sun, M. Mann, A. S. Tang, M. C. Onbasli, D. Bono, P. M. Voyles, Y. Xu, *et al.*, $Tm_3Fe_5O_{12}$/Pt Heterostructures with perpendicular magnetic anisotropy for spintronic applications, Adv. Electron. Mater. **3,** 1600376 (2017).

[16] J. J. Bauer, E. R. Rosenberg, S. Kundu, K. A. Mkhoyan, P. Quarterman, A. J. Grutter, B. J. Kirby, J. A. Borchers, and C. A. Ross, Dysprosium iron garnet thin films with perpendicular magnetic anisotropy on silicon, Adv. Electron. Mater. **6,** 1900820 (2020).

[17] M. L. Néel, Propriétés magnétiques des ferrites; ferrimagnétisme et antiferromagnétisme, Ann. Phys. (Paris) **12,** 137 (1948).

[18] A. E. Clark and E. Callen, Néel ferrimagnets in large magnetic fields, J. Appl. Phys. **39,** 5972 (1968).

[19] G. F. Dionne, Molecular field coefficients of substituted yttrium iron garnets, J. Appl. Phys. **41,** 4874 (1970).

[20] C. D. Brandle and S. L. Blank, Magnetic moments for mixed substituted rare earth iron garnets, IEEE Trans. Magn. **12,** 14 (1976).

[21] G. F. Dionne, Origin of exchange field reductions in diluted magnetic garnets, J. Appl. Phys. **85,** 4627 (1999).

[22] G. F. Dionne and P. F. Tumelty, Molecular-field coefficients of $Tm_3Fe_5O_{12}$, J. Appl. Phys. **50,** 8257 (1979).

[23] G. F. Dionne, Molecular-field coefficients of rare-earth iron garnets, J. Appl. Phys. **47,** 4220 (1976).

[24] G. F. Dionne, Molecular field and exchange constants of Gd3+- substituted ferrimagnetic garnets, J. Appl. Phys. **42,** 2142 (1971).

[25] G. F. Dionne, *Magnetic Moment Versus Temperature Curves of Rare-Earth Iron Garnets* (MIT Lincoln Laboratory Technical Report, Lexington, 1979).

[26] E. E. Anderson, J. R. Cunningham, and G. E. McDuffie, Magnetic properties of the mixed garnets $(3 − x)Y_2O_{3 \bullet x}$ $Gd_2O_{3 \bullet 5}Fe_2O_3$, Phys. Rev. **116,** 624 (1959).

[27] G. Villers, J. Loriers, and C. Claudel, Magnetisme – quelques proprietes des grenats mixtes de gadolinium-erbium et de gadolinium-yttrium, C. R. Acad. Sci. **247,** 710 (1958).

[28] A. Vassiliev, J. Nicolas, and M. Hildebrandt, Magnétisme – sur les proprietes des grenats mixtes d'yttrium-holmium, C. R. Acad. Sci. **253,** 242 (1961).

[29] A. Vassiliev, J. Nicolas, and M. Hildebrandt, Magnétisme – sur les proprietes des grenats mixtes d'yttrium-gadollinium, C. R. Acad. Sci. **252,** 2529 (1961).

[30] A. Vassiliev, J. Nicolas, and M. Hildebrandt, Magnétisme – Sur les proprietes des grenats mixtes d'yttrium-dysprosium, C. R. Acad. Sci. **252,** 2681 (1961).

[31] S. Geller, J. P. Remeika, R. C. Sherwood, H. J. Williams, and G. P. Espinosa, Magnetic study of the heavier rare-earth iron garnets, Phys. Rev. **137,** A1034 (1965).

[32] G. R. Harrison and L. R. Hodges, Temperature stable microwave hybrid garnets, J. Appl. Phys. **33,** 1375 (1962).

[33] R. Pauthenet, Spontaneous magnetization of some garnet ferrites and the aluminum substituted garnet ferrites, J. Appl. Phys. **29,** 253 (1958).

[34] R. Pauthenet, Magnetic properties of the rare earth garnets, J. Appl. Phys. **30,** S290 (1959).

[35] R. Pauthenet, Les propriétés magnétiques des ferrites d'yttrium et de terres rares de formule $5Fe_2O_{3.3}M_2O_3$, Ann. Phys. (Paris) **13,** 424 (1958).

[36] T. Su, S. Ning, E. Cho, and C. A. Ross, Magnetism and site occupancy in epitaxial Y-rich yttrium iron garnet films, Phys. Rev. Mater. **5,** 094403 (2021).

[37] G. F. Dionne, *Magnetic Oxides* (Springer, New York, US, 2009).

[38] E. Rosenberg, J. Bauer, E. Cho, A. Kumar, J. Pelliciari, C. A. Occhialini, S. Ning, A. Kaczmarek, R. Rosenberg, J. W. Freeland, *et al.*, Revealing site occupancy in a complex oxide: terbium iron garnet, Small **19,** 2300824 (2023).

[39] G. F. Dionne, Molecular-field coefficients of $MnFe_2O_4$ and $NiFe_2O_4$ spinel ferrite systems, J. Appl. Phys. **63,** 3777 (1988).

[40] G. F. Dionne, High magnetization limits of spinel ferrite, J. Appl. Phys. **61,** 3865 (1987).

[41] B. Tomasello, D. Mannix, S. Geprägs, and T. Ziman, Origin and dynamics of umbrella states in rare-earth iron garnets, Ann. Phys. (N. Y.) **447,** 169117 (2022).

[42] A. Boutaba, M. Lahoubi, V. Varazashvili, and S. Pu, Magnetic, magneto-optical and specific heat studies of the low temperature anomalies in the magnetodielectric DyIG ferrite garnet, J. Magn. Magn. Mater. **476,** 551 (2019).

[43] J. Cieslak, M. Reissner, J. Dabrowa, and K. Zielinska, Magnetization measurements of multicomponent iron garnets, J. Magn. Magn. Mater. **582,** 170987 (2023).

[44] V. Joch, P. Molho, and L. Ranno, magnetization processes in a dot of ferrimagnetic garnet near the compensation temperature, J. Phys.: Conf. Ser. **303,** 012006 (2011).

[45] J. Bernasconi and D. Kuse, Canted spin phase in gadolinium iron garnet, Phys. Rev. B **3,** 811 (1971).

[46] E. E. Anderson, Molecular field model and the magnetization of YIG, Phys. Rev. **134,** A1581 (1964).

[47] R. Z. Levitin, B. K. Ponomarev, and Y. F. Popov, Magnetization of iron garnets of heavy rare earth elements in fields up to 240 kOe, Sov. Phys. JETP **59,** 1952 (1971).

[48] W. Wang, R. Chen, and X. Qi, Analysis on three-sublattice model of magnetic properties in rare-earth iron garnets under high magnetic fields, J. Alloys Compd. **512,** 128 (2012).

[49] A. Budkowski, A. Szytuła, D. Rodic, R. Duraj, J. Mayer, J. Sciesinski, and V. Spasojevic, The compensation point in reig and some of its properties, J. Magn. Magn. Mater. **78,** 226 (1989).

[50] P. Virtanen, R. Gommers, T. E. Oliphant, M. Haberland, T. Reddy, D. Cournapeau, E. Burovski, P. Peterson, W. Weckesser, J. Bright, *et al.*, SciPy 1.0: fundamental algorithms for scientific computing in python, Nat. Methods **17,** 261 (2020).

[51] https://github.com/mjgross20/DIONNE

[52] R. Aléonard, Etude paramagnetique des ferrites d'yttrium et de terres rares de formule $5Fe_2O_3 \cdots 3M_2O_3$, J. Phys. Chem. Solids **15,** 167 (1960).

[53] W. P. Wolf and J. H. Van Vleck, Magnetism of europium garnet, Phys. Rev. **118** (1960).

[54] M. Binder, A. Weber, O. Mosendz, G. Woltersdorf, M. Izquierdo, I. Neudecker, J. R. Dahn, T. D. Hatchard, J. U. Thiele, C. H. Back, *et al.*, Magnetization dynamics of the ferrimagnet CoGd near the compensation of magnetization and angular momentum, Phys. Rev. B: Condens. Matter Mater. Phys. **74,** 134404 (2006).

[55] S. A. Siddiqui, J. Han, J. T. Finley, C. A. Ross, and L. Liu, Current-induced domain wall motion in a compensated ferrimagnet, Phys. Rev. Lett. **121,** 057701 (2018).

[56] B. A. Calhoun, W. V. Smith, and J. Overmeyer, Ferrimagnetic resonance in gadolinium iron garnet, J. Appl. Phys. **29,** 427 (1958).

[57] M. A. Gilleo and S. Geller, Magnetic and crystallographic properties of substituted yttrium-iron garnet, $3Y_2O_3 \cdot xM_2O_3 \cdot (5 - x)Fe_2O_3$, Phys. Rev. **110,** 73 (1958).

[58] E. Baños-López, C. A. Cortés-Escobedo, F. Sánchez-De Jesús, A. Barba-Pingarrón, and A. M. Bolarín-Miró, Crystal structure and magnetic properties of cerium-doped YIG: effect of doping concentration and annealing temperature, J. Alloys Compd. **730,** 127 (2018).

[59] V. Sharma and B. K. Kuanr, magnetic and crystallographic properties of rare-earth substituted yttrium-iron garnet, J. Alloys Compd. **748,** 591 (2018).

[60] G. P. Espinosa, Crystal chemical study of the rare-earth iron garnets, J. Chem. Phys. **37,** 2344 (1962).

[61] W. A. Bonner, A novel Non-Pb flux system for the preparation of yttrium and rare earth iron gallium and aluminum garnets, Mater. Res. Bull. **12,** 289 (1977).

[62] A. Paoletti, *Physics of Magnetic Garnets* (North-Holland Pub. Co., Amsterdam, 1979).

[63] S. A. Manuilov, S. I. Khartsev, and A. M. Grishin, Pulsed laser deposited $Y_3Fe_5O_{12}$ films: nature of magnetic anisotropy i, J. Appl. Phys. **106,** 123917 (2009).

[64] Y. Dumont, N. Keller, E. Popova, D. S. Schmool, S. Bhattacharya, B. Stahl, M. Tessier, and M. Guyot, Superexchange and iron valence control by off-stoichiometry in yttrium iron garnet thin films grown by pulsed laser deposition, J. Appl. Phys. **97,** 10G108 (2005).

[65] S. Damerio and C. O. Avci, Sputtered terbium iron garnet films with perpendicular magnetic anisotropy for spintronic applications, J. Appl. Phys. **133,** 073902 (2023).

[66] See Supplemental Material at http://link.aps.org/supplemental/10.1103/PhysRevApplied.21.014060 for additional examples of DIONNE and details of the formulas used in the model.